ACSNANO

www.acsnano.org

ARTICLE

Even-Parity Self-Trapped Excitons Lead to Magnetic Dipole Radiation in Two-Dimensional Lead Halide Perovskites

Ryan A. DeCrescent, Xinhong Du, Rhys M. Kennard, Naveen R. Venkatesan, Clayton J. Dahlman, Michael L. Chabinyc, and Jon A. Schuller*

Cite This: *ACS Nano* 2020, 14, 8958–8968

Read Online

ACCESS | Metrics & More | Article Recommendations | Supporting Information

ABSTRACT: Recently, unconventional bright magnetic dipole (MD) radiation was observed from two-dimensional (2D) hybrid organic–inorganic perovskites (HOIPs). According to commonly accepted HOIP band structure calculations, such MD light emission from the ground-state exciton should be strictly symmetry forbidden. These results suggest that MD emission arises in conjunction with an as-yet unidentified symmetry-breaking mechanism. In this paper, we show that MD light emission originates from a self-trapped p-like exciton stabilized at energies below the primary electric dipole (ED)-emitting 1s exciton. Using suitable combinations of sample and collection geometries, we isolate the distinct temperature-dependent properties of the ED and MD photoluminescence (PL). We show that the ED emission wavelength is nearly constant with temperature, whereas the MD emission wavelength exhibits substantial red shifts with heating. To explain these results, we derive a microscopic model comprising two distinct parity exciton states coupled to lattice distortions. The model explains many experimental observations, including the thermal red shift, the difference in emission wavelengths, and the relative intensities of the ED and MD emission. Thermodynamic analysis of temperature-dependent PL reveals that the MD emission originates from a locally distorted structure. Finally, we demonstrate unusual hysteresis effects of the MD-emitting state near structural phase transitions. We hypothesize that this is another manifestation of the local distortions, indicating that they are insensitive to phase changes in the equilibrium lattice structure.

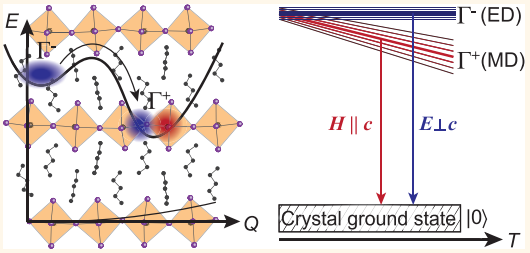

KEYWORDS: *2D materials, hybrid perovskites, momentum-resolved spectroscopies, excitons, electric dipoles, magnetic dipoles, optical anisotropies, polarons*

Hybrid organic–inorganic perovskites (HOIPs) are a burgeoning class of solution-processable semiconductor materials with high-quality optoelectronic properties.[1,2] Two-dimensional (2D) HOIPs (*e.g.*, Ruddlesden–Popper phases) offer enhanced environmental stability and additional structural, chemical, quantum-mechanical, and dielectric degrees of freedom for tailoring the optoelectronic properties.[3−8] These systems have been widely exploited to explore fundamental physics,[8−13] structure–function relationships,[7] and synthetic chemistry techniques.[14]

Compared to their 3D counterparts, 2D HOIPs exhibit new and unexpected spectral features,[15] particularly in photoluminescence (PL).[4,16−19] For example, broad, low-energy "white-light"-emitting states are common in ⟨110⟩-oriented ("corrugated") perovskite structures and are currently attributed to deep exciton self-trapping in the soft ionic lattice.[16,20] Planar ⟨100⟩-oriented systems also exhibit an unexpected PL sideband at room temperature.[4,13,17−19,21] Unlike the white-light-emitting states, this sideband is spectrally narrow (comparable to the primary exciton) and separated from the primary exciton by only ∼100 meV (compared to ∼1 eV for white-light states). This feature appears with widely varying strength in the existing literature and is seemingly absent in some reports,[22,23] leading to widely variable interpretations.[18,21,24]

In a recent report, we demonstrated that the low-energy sideband in planar 2D HOIPs arises from an unconventionally fast magnetic dipole (MD) transition.[13] As seen in momentum-resolved PL, this vertically oriented MD transition emits s-polarized light primarily into highly oblique angles.[13]

Received: May 6, 2020
Accepted: July 8, 2020
Published: July 15, 2020

https://dx.doi.org/10.1021/acsnano.0c03783
ACS Nano 2020, 14, 8958–8968

Therefore, depending on the collection geometry (Figure 1a) and numerical aperture (NA), the MD emission may not be

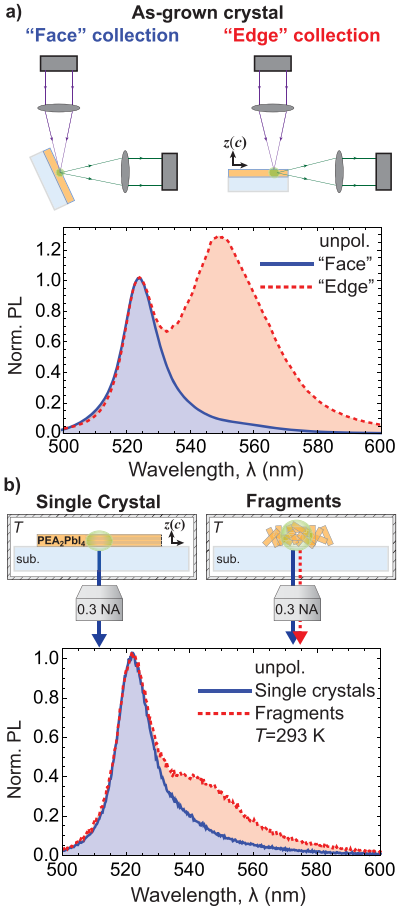

Figure 1. Geometry dependence of PL spectra from single crystals of PEA_2PbI_4. (a) With a conventional experimental geometry, the MD emission can be resolved as a pronounced low-energy emission peak when collecting PL from the edge of the crystal (right; red dotted curve), *i.e.*, perpendicular to the crystal *c*-axis. The MD is absent in PL spectra collected from the crystal face (left; solid blue curve). (b) Schematic of an experimental scheme to isolate and measure the temperature dependence of ED and MD emission while controlling the sample temperature. PL is measured from samples in a temperature-controlled cryostat using an NA = 0.3 objective. PL from oriented single crystals (left; solid blue curve) again shows only the single ED emission peak. PL from an ensemble of crystalline flakes with random orientations (right; dotted red curve) shows both ED and MD emission. All spectra are unpolarized.

visible or may appear as a prominent sideband, explaining existing discrepancies in the literature. This discovery of MD PL is both generally surprising—it is the only known case of MD emission in an extended crystal—and specifically perplexing—MD radiation from the band-edge 1s exciton in 2D HOIPs is formally parity forbidden.[5,25] Here, we propose that the MD emission originates from a ground-state exciton polaron comprising a self-trapped odd-parity excitonic Rydberg state (*e.g.*, 2p). Specifically, we focus upon phenethylammonium lead iodide (PEA_2PbI_4) and exploit sample orientation, experimental geometry, and polarization to isolate the distinct electric dipole (ED)-emitting and MD-emitting states using conventional spectroscopies. We study the peak wavelengths, widths, relative PL intensities, and decay dynamics as a function of temperature. We adopt a model from Noba *et al.*, consisting of an exciton with two internal states, s (even) and p (odd), coupled with stabilizing lattice distortions.[26] Through suitable choice of the model parameters, we quantitatively explain experimentally observed thermal red shifts, ED/MD energy splittings, and relative ED/MD intensities over a broad temperature range. The effect is not specific to PEA_2PbI_4 but also exists in related systems, such as butylammonium lead iodide (BA_2PbI_4). In BA_2PbI_4, we additionally discover unusual hysteresis behavior of the MD emission around structural phase transitions. This mechanistic framework may thus point toward ways of engineering these light−matter interactions, and our experimental methodologies make future studies *via* conventional spectroscopies easily accessible.

RESULTS AND DISCUSSION

MD Emission and Excitonic Rydberg States. First, we establish the foundations whereby MD emission may derive from ordinarily high-energy Rydberg states of the exciton. Building from a similar treatment described in the Supporting Information of ref 13, here, we provide further discussion clarifying the details and origins of all relevant terms. Consider a crystal point group described by irreducible representation Γ. The selection rules for excitonic transitions are determined by the direct product

$$\Gamma_s \otimes \Gamma' \otimes \Gamma_X \tag{1}$$

where Γ_s, Γ', and Γ_X are irreducible representations, respectively, of the crystal ground state (the totally symmetric representation), the operator mediating the transition (*e.g.*, ED or MD operators), and the exciton state.[27−29] The exciton state further transforms according to the symmetries of the electron (Γ_e), hole (Γ_h), and envelope function (Γ_f), that is, $\Gamma_X = \Gamma_f \otimes \Gamma_e \otimes \Gamma_h$.[29] Assuming a D_{4h} crystal point group, the electron at the conduction band minimum and hole at the valence band maximum transform as E_u and A_{1g}, respectively.[5] The in-plane ED operator and *z*-oriented MD operator transform as E_u and A_{2g}, respectively. The s-like envelope function and the crystal ground state also transform as A_{1g}. By the vanishing integral rule of group theory, the transition is allowed if the direct product in eq 1 contains $\Gamma_s = A_{1g}$. We thus evaluate for the MD operator and the 1s exciton state:

$$A_{1g} \otimes A_{2g} \otimes (A_{1g} \otimes E_u \otimes A_{1g}) \not\supset A_{1g} \tag{2}$$

which shows that the 1s exciton cannot radiate through a *z*-oriented MD transition. Although various static (*e.g.*, octahedral tilting or metal off-centering) or dynamic (*e.g.*, thermal disorder) symmetry-breaking mechanisms[30−35] could relax these selection rules, they would lead to mixed-parity transitions rather than the experimentally observed pure ED or MD emission channels.

In contrast, the in-plane p-like exciton Rydberg state ($\Gamma_f = E_u$) can radiate through a *z*-oriented MD channel:

$$A_{1g} \otimes A_{2g} \otimes (E_u \otimes E_u \otimes A_{1g}) \supset A_{1g} \tag{3}$$

The unperturbed (hydrogenic) 2p exciton state should lie at energies above the 1s exciton (≈300 meV for this material).[36] It is thermodynamically unstable and inconsistent with our experimental observations of an MD emission feature ≈90 meV below the 1s exciton at room temperature.[13] However, strong exciton−phonon coupling in ionic crystals leads to

https://dx.doi.org/10.1021/acsnano.0c03783
ACS Nano 2020, 14, 8958−8968

dynamic lattice relaxations that can stabilize photoexcitations to lower energies.[15,37−40] This phenomenon has been invoked to explain white-light-emitting states in 2D HOIPs[16] and other broad sub-band-gap emission in organic crystals.[41] In 2D HOIPs, recent numerical calculations suggest the possibility of an "off-site" (parity-broken) self-trapped exciton (STE), in which the electron and hole are stabilized in a p-like configuration on adjacent cells of the crystal.[40] Similarly, earlier theoretical[26,37,42] and experimental[43] reports demonstrate the prevalence of such off-center relaxation of STEs in alkali halides. In many related studies, investigations of temperature-dependent PL reveal insights into the nature of STEs in 2D HOIPs,[20,44] alkali halides,[45] and organic crystals.[41] Unlike these previous studies, here, we can use a suitable choice of experiment and sample geometry to selectively isolate the temperature dependence of the ED and MD emission.

Isolating ED and MD Emission *via* Experimental Geometry. Single crystals of 2D HOIPs (*e.g.*, PEA_2PbI_4), when grown from solution on a substrate, tend to grow with the crystalline *c*-axis (the layering direction, or "long axis") perpendicular to the substrate, such that the lead iodide sheets are highly oriented parallel to the substrate interface (Methods and Figure S1).[46] The ED and MD emission features can be distinguished using momentum-resolved spectroscopies (Figure S2).[13] Reference 13 establishes the basic polarization, angular, and spectral characteristics of these two features in alkylammonium lead iodide 2D HOIPs. Here, we establish the same basic features also in PEA_2PbI_4. The ED-mediated exciton emission appears as a single 525 nm peak (Figure S2), regardless of experimental geometry. The MD emission, in contrast, is observed around 550 nm only in s-polarized spectra and predominantly beyond the critical angle of total internal reflection.

To develop a configurational coordinate model for the system, we wish to study the temperature dependence of these distinct emission features. However, immersion fluids required for high-NA imaging preclude the use of momentum-resolved methods to distinguish ED and MD emission away from room temperature. We instead use a conventional experimental geometry and manipulate the crystal orientation with respect to the collection optics. This strategy is summarized in Figure 1a, which shows spectra as collected from the "face" (blue; left schematic) or "edge" (red; right schematic) of a broad as-grown crystal of PEA_2PbI_4 on a glass coverslip (Methods).[46] Face-collected spectra (blue) show a single 525 nm ED peak, whereas edge-collected spectra (red) reveal the distinct low-energy MD emission around 550 nm. Similar measurements on BA_2PbI_4 crystals reveal nearly identical behavior, albeit with different relative intensities and peak wavelengths (Figure S3). Importantly, this indicates that the emission does not originate from crystal edges but rather propagates toward the edges from the bulk of the crystal.

This approach offers several notable benefits: measurements are performed on largely undisturbed crystals; individual crystals remain highly oriented, and therefore, the spectral features can be further isolated by means of a linear polarizer (Methods); it obviates the need for immersion oils in variable-temperature experiments. However, it requires a cryostat with orthogonal excitation and collection windows. Later, we use this geometry to measure PL decay dynamics. To continuously collect temperature-dependent spectra, we instead use crystal reorientation to selectively probe ED and MD emission within a cryostat with collinear collection and excitation, that is, both along the substrate *z*-axis with a 0.3 NA objective (Figure 1b and Methods). To probe ED-mediated exciton emission, we selectively excite single as-grown crystals of PEA_2PbI_4 (left schematic) at low power (≈0.05 mW/cm^2) with a loosely focused 405 nm laser. The room-temperature spectra (blue) exhibit the single narrow ED exciton centered around 525 nm. To probe MD emission, we fracture the large single crystals and collect the fragments on a secondary substrate (right schematic; Methods). The resulting room-temperature PL spectrum (red) shows two distinct emission features, consistent with both momentum-resolved PL (Figure S2) and edge measurements of single crystals (Figure 1a). The relative strengths differ significantly between Figure 1a,b because the PL from the randomly oriented ensemble of fragments emulates collection from all angles with respect to a single crystal. Nonetheless, the overall similarity indicates that the relevant photophysics is insensitive to the fracturing process. Below, we use these geometries to demonstrate how ED and MD emission wavelengths, widths, intensities, and dynamics vary with temperature (Methods).

Temperature-Dependent Photoluminescence. Using the aforementioned approach, PL spectra are collected continuously while the sample temperature is varied. Temperature-dependent PL spectra from the ensemble of fragments are plotted in Figure 2a for temperatures between 175 and 360 K. The spectra are normalized such that the total collected PL is equivalent at each temperature. No abrupt changes associated with structural phase transitions are observed between 77 and 400 K, consistent with previous reports and reflecting the mechanical and thermal stability of PEA_2PbI_4 compared to that with similar materials prepared with other organic cations.[21,47] The peak wavelength and full width at half-maximum (fwhm) of the ED emission are quite stable, as expected for excitonic properties that depend principally on the static electronic structure. Indeed, the behavior of the ED emission observed here matches that from as-grown crystals (Figure S4). The MD emission, on the other hand, exhibits a dramatic temperature dependence with a thermal red shift of approximately 30 nm (approximately 120 meV) over the presented temperature range. This large thermal red shift excludes extrinsic defects as a likely origin for the MD emission, as these typically have a well-defined energy with respect to the electronic bands. Instead, the thermal red shifts provide strong evidence that the MD emission originates from STEs, as similar behavior has previously been observed in STEs in lithium niobate[39] and perylene.[41]

We quantify this behavior by first analyzing as-grown single-crystal PL, where the fit parameters for the ED (*i.e.*, amplitude, width, and center) can be confidently determined in the absence of additional PL features. These results are then used to eliminate free parameters from the ensemble PL, which requires a two-peak model. In this way, we minimize concerns of parameter correlations in fits of the ensemble PL data (Methods), especially at the lowest temperatures where the features strongly overlap.

The temperature-dependent ED and MD emission wavelengths are summarized in Figure 2b. Notably, the observed energy difference between the ED (blue circles) and MD (red squares) emission, $\Delta E(T)$, increases approximately linearly at increased temperatures (Figure 2b inset). The fwhm values of both emission features are nearly identical at 170 K (Figure 2c). Below 170 K, the ED and MD peaks strongly overlap

https://dx.doi.org/10.1021/acsnano.0c03783
ACS Nano 2020, 14, 8958−8968

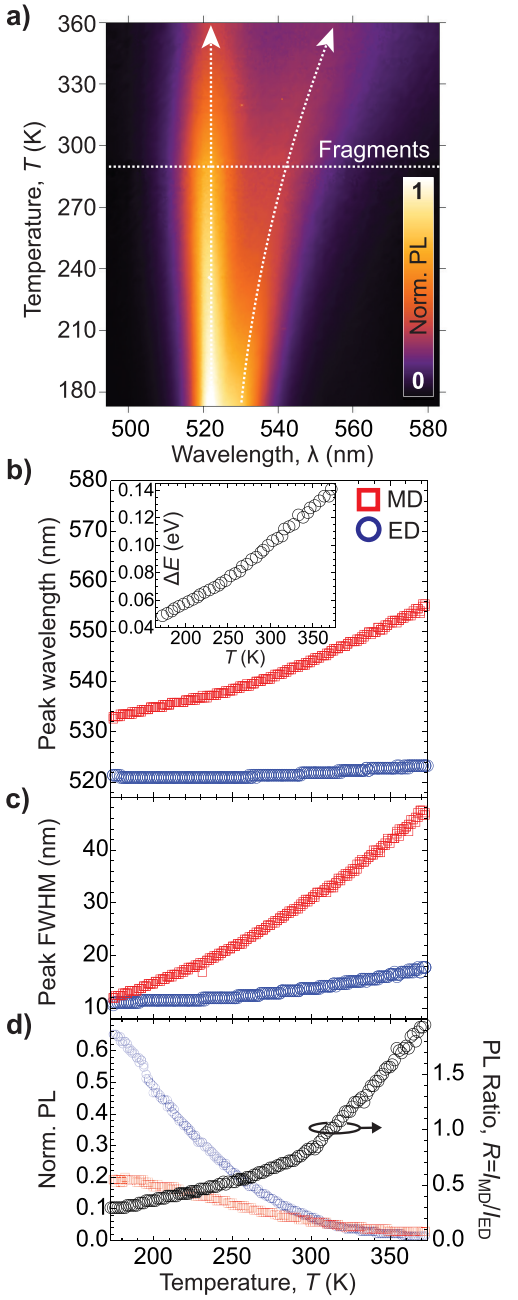

Figure 2. Temperature-dependent PL spectra of PEA_2PbI_4. (a) Temperature-dependent PL spectra from randomly oriented fragments, as shown in Figure 1b. Vertical white arrows are qualitative guides for the eye; the horizontal white dashed line corresponds to the spectral line cuts shown in Figure 1b. Spectra have been normalized at each temperature to retain clarity of the emission features over the entire temperature range. (b) Peak wavelengths of the ED and MD PL features. Inset: Observed PL energy difference, ΔE. (c) Full width at half-maximum of the ED and MD emission features derived from single crystal and fragment data, respectively. (d) (Black circles) Ratio of integrated MD PL over the integrated ED PL, $R(T) = I_{MD}(T)/I_{ED}(T)$ (right axis scale), derived from two-component fits to fragments data. Colored markers show the individual integrated ED and MD PL results (left axis scale). All subpanels: red squares = MD; blue circles = ED.

(Figure S4), complicating unique determination of the parameters of interest. Nonetheless, the ED fwhm is clearly far more stable with temperature than that of the MD, further reflecting the latter's relation to variations in the local atomic structure.

To understand the energetic landscape of the two states, we quantify the total (spectrally integrated) ED and MD emission intensities as a function of temperature. The integrated PL from both the ED and MD decreases exponentially with increasing temperature (Figure 2d, red and blue markers; Figure S4), reflecting thermally activated nonradiative relaxation. However, the relative integrated PL (Figure 2d, black circles) shows an uncommon behavior. As the temperature increases, the relative intensity of the MD PL (red squares) grows significantly, contributing equally with the ED PL (blue circles) at approximately 315 K and exceeding the ED PL at higher temperatures. Next, we detail a simple exciton–lattice coupling model to explain the origins of these behaviors and to show that the relative intensities are consistent with simple thermodynamic considerations once the self-trapping depth is properly quantified.

Origin of the Thermal Variations. Temperature-dependent PL is frequently used to derive configurational-coordinate energy diagrams which ultimately reflect exciton–lattice interactions[48,49] and govern thermally activated population exchange.[20,40,41,44,50] For example, temperature-dependent PL ratios have been used to estimate the exciton self-trapping depth in organic crystals[41] and white-light-emitting 2D HOIPs.[20,44] Here, this type of analysis is complicated by the significant variation in the observed energy difference, $\Delta E(T)$, between the emission features (*e.g.*, Figure 2b inset; Figure S5). For example, as ΔE increases at constant temperature, the thermal occupancy of the low-energy (MD) state is expected to increase relatively. In competition, increasing temperature tends to increase the occupation of the high-energy (ED) state. The experimental trend thus depends on the detailed balance between these two effects. In this particular case, the rate of change of $\Delta E(T)$, $d(\Delta E)/dT \approx 5.5k_B$ (k_B is the Boltzmann constant), exceeds the rate of change of thermal energy, $d(k_BT)/dT = k_B$ (Figure S5). One thus expects the MD emission to grow in relative intensity with increasing temperature.

The ED and MD PL intensities, $I_{ED}(T)$ and $I_{MD}(T)$, are generated from distinct exciton populations, $N_{ED}(T)$ and $N_{MD}(T)$, with distinct radiative rates, Γ_{ED} and Γ_{MD}, respectively:[28]

$$I_{ED}(T) = c_{exp}N_{ED}(T)\Gamma_{ED} \tag{4}$$

$$I_{MD}(T) = c_{exp}N_{MD}(T)\Gamma_{MD} \tag{5}$$

Here, c_{exp} accounts for temperature-independent collection efficiencies. If the exciton populations are in thermal equilibrium, variations in the ratio of PL intensities, $R(T) = I_{MD}(T)/I_{ED}(T)$, are described by Boltzmann statistics:[20,41,44]

$$R(T) = \frac{\Gamma_{MD}}{\Gamma_{ED}} \times \frac{N_{MD}(T)}{N_{ED}(T)} = \frac{\Gamma_{MD}}{\Gamma_{ED}} \times e^{G/k_BT} \tag{6}$$

Here, G represents the positive self-trapping depth, that is, the *true* energy difference between the two states in the excited-state manifold[41] (*e.g.*, see Figure 3c). Critically, there is a distinction between G and the *observed* energy difference of emission, ΔE. In general, G and ΔE differ because the transitions occur at different points in the ground-state manifold with different configurational energies.[41] In the

https://dx.doi.org/10.1021/acsnano.0c03783
ACS Nano 2020, 14, 8958–8968

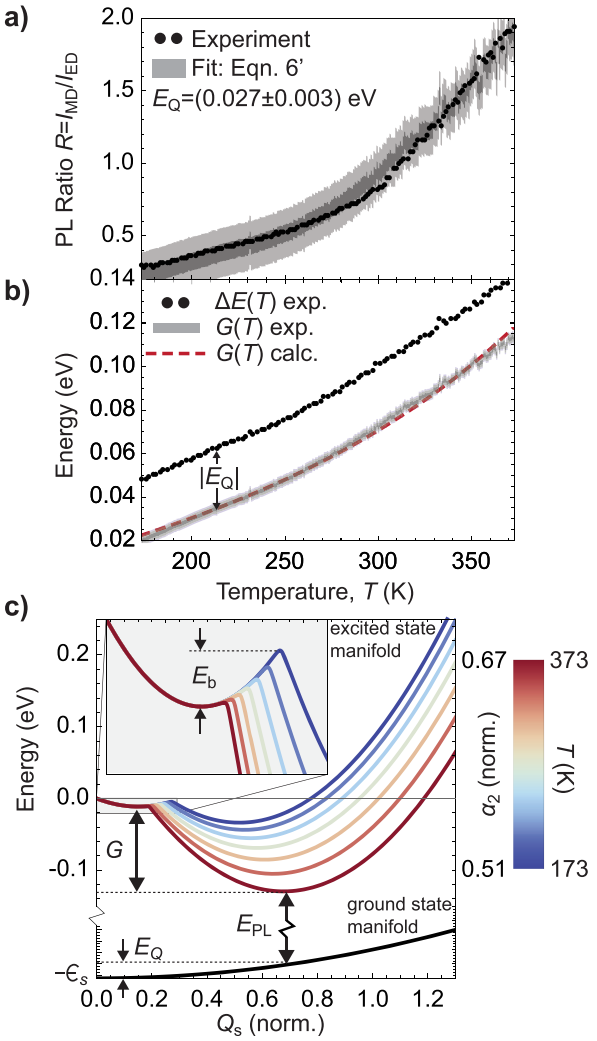

Figure 3. Modeling the energetics of ED and MD emission. (a) PL ratio, $R(T) = I_{MD}(T)/I_{ED}(T)$. Black markers: Experiment. Gray filled region: Fit to experiment using eq 6′ with E_Q = 0.027 eV. (b) (Black markers) PL energy difference, $\Delta E(T)$, and (gray filled region) true energy difference, $G(T)$. Red dashed line: Calculated $G(T)$ curve using the exciton−lattice coupling model discussed in this section assuming $\alpha_2(T) \propto 1/\sqrt{k(T)}$ (where k is the elastic constant, described in main text), α_1 = 0.15, and β = 0.15. In (a,b), dark- and light-gray regions represent 1σ and 3σ confidence intervals, respectively. (c) Configurational-coordinate diagram generated from the exciton−lattice coupling model. The excited-state manifold (colored curves) is the low-energy eigenvalue of eq 7 and is plotted for various temperatures (α_1 = 0.15 and β = 0.15). Line cuts were taken at Q_p = 0.005. Illustrated energy quantities are described in the main text. The color scale for α_2 is not linear. Q_p, Q_s, α_1, α_2, and β are in units of eV$^{1/2}$; see Supporting Information S2.

current context, the two distinct excited states relax to ground-state configurations that differ by an energy E_Q (*i.e.*, $\Delta E(T) = G(T) + E_Q$).

Notably, the experimentally observed ratio $R(T)$ from PEA_2PbI_4 (Figure 2d) cannot be explained by any constant value of G. We expect G to vary with temperature in a manner similar to ΔE. The simplest assumption is that the ground-state configurational energy, E_Q, is temperature-independent, leading to a revised form of eq 6:

$$R(T) = \frac{\Gamma_{MD}}{\Gamma_{ED}} \times e^{[\Delta E(T) - E_Q]/k_B T} \quad (6')$$

Essentially, eq 6′ allows us to estimate the true exciton trapping depth, $G(T)$, from experimentally determined $\Delta E(T)$ and $R(T)$. Indeed, eq 6′ provides a very good description of the experimentally observed $R(T)$ with a constant value of E_Q = 0.027 ± 0.003 eV (Figure 3a). The resulting function $G(T)$, shown in Figure 3b (gray filled region), is always less than $\Delta E(T)$ (black markers). Although $G(T)$ varies with temperature, $G(T) > 0$ over the entire temperature range studied here, consistent with a stable trapped state. Physically, $E_Q > 0$ corresponds to the positive ground-state energy of a local lattice distortion. This is strong quantitative evidence that the MD emission originates from a locally distorted lattice structure.

The origins of $G(T)$, E_Q, and a low-energy, p-like exciton are succinctly described in a model adapted from Noba *et al.*[26] Consider two distinct exciton states of opposite parity, s (even) and p (odd), coupled to two distinct lattice distortions of opposite parity described by normalized amplitudes Q_s (symmetric) and Q_p (antisymmetric). Nominally, s and p are associated with 1s and 2p exciton states. Here, they correspond to ED and MD emission features, respectively. We adopt a simplified two-state model and write the 2 × 2 Hamiltonian (Supporting Information S1):[26]

$$H = \begin{pmatrix} \epsilon_s - \alpha_1 Q_s + Q^2/2 & -\beta Q_p \\ -\beta Q_p & \epsilon_p - \alpha_2 Q_s + Q^2/2 \end{pmatrix} \quad (7)$$

where ϵ_s (ϵ_p) is the energy of the unperturbed s (p) exciton, $Q^2 = Q_s^2 + Q_p^2$, α_1 (α_2) is the s-Q_s (p-Q_s) coupling constant, and β is the coupling constant that mixes s and p exciton states through the antisymmetric distortion Q_p.

Because the $Q_{s,p}$ are normalized coordinates, the "softness" of the crystal is contained in the coupling parameters,[26] which are thus generally temperature-dependent (see Supporting Information S2 for a discussion about units and temperature variations). Eigenenergies, E_1 and E_2, are obtained by diagonalizing H, yielding configurational-coordinate energy diagrams in the variables Q_s and Q_p. With insight from experiments, we constrain the model parameters and reproduce the essential experimental observations (Supporting Information S1).

Illustrative results from this model are shown in Figure 3c, where the lowest energy eigenvalue is plotted as a function of Q_s at various temperatures (colored curves). Experimentally measured PL wavelengths and Stokes shifts (≈23 meV) for the ED exciton yield the parameter value α_1 = 0.15 eV$^{1/2}$ (Supporting Information S1). Symmetry considerations suggest that β is small compared to the remaining free parameter, α_2; β determines the mixing of exciton parities (Supporting Information S1 and Figure S6), but experimentally, we observe emission features with well-defined parity[13] and no evidence for mixing. Consequently, α_1 and α_2 are the relevant system parameters (and thus Q_s the relevant distortion) for modeling our experimental results (Figure S7). The ground-state energy (solid black curve) exhibits a simple quadratic dependence: $E_g \sim Q_s^2/2$. As is common in the Born−Oppenheimer approximation, the ED PL peak is represented by vertical transitions at nonzero values of the configuration coordinate ($Q_s \approx 0.12$ eV$^{1/2}$). Though the charge

https://dx.doi.org/10.1021/acsnano.0c03783
ACS Nano 2020, 14, 8958−8968

configuration associated with the MD emission is likely not identical to that of the 2p exciton, experimental inferences of the 2p exciton energy[36] suggest a starting guess of $\epsilon_p - \epsilon_s \approx 0.3$ eV. Further refinements favor a smaller value of $\epsilon_p - \epsilon_s \approx 0.1$ eV (Figure S8).

At larger values of Q_s, global minima appear and are associated with a p exciton stabilized by the lattice distortion. The MD emission originates from a vertical transition from this global minimum of the excited-state manifold to the ground-state manifold. Compared to the ED emission, the MD emission occurs at $Q_s \approx 0.6$ eV$^{1/2}$, where $E_Q \approx 27$ meV. At each temperature, we solve for the value of $\alpha_2(T)$ that corresponds to the experimentally observed trapping depth, $G(T)$ (Figure S9). Excellent agreement is obtained by assuming that the elastic modulus, $k(T)$, decreases linearly with temperature (Figure 3b, red dashed line), as expected in crystalline solids far from extreme temperatures (*e.g.*, deep cryogenic or near-melting) (Supporting Information S2).[51,52] Finally, the experimentally measured values of E_Q determine the relative ground-state spring constant (*i.e.*, curvature of the ground-state manifold) (Supporting Information S1).

The deepening of the global minimum is naturally accompanied by a reduced energy barrier, E_b, between the two minima (Figure 3c, inset). Values of E_b determined from these model parameters vary between ~1 and 8 meV, less than the thermal energy (k_BT) for all temperatures considered in the analysis thus far. Therefore, rapid thermal energy transfer from the ED to the MD state is expected. As a result, ED and MD PL traces (Methods) exhibit nearly identical decay dynamics (Figure 4a, left panel). However, as temperatures drop below approximately 170 K, k_BT becomes comparable to or less than the energy barrier, and distinct decay dynamics are resolved (Figure 4a, right panel). Decay traces at all temperatures are well-modeled by biexponential decay with a short (nanosecond scale) component and a long-lived (~20 ns) component, similar to previous reports (Figures S10 and S11).[50,53] Results are summarized in Figure 4b. PL lifetimes begin to significantly diverge below approximately 200 K, as expected from the theoretical model. Overall decreasing PL lifetimes at higher temperatures likely reflect overall decreasing PL quantum yields (black curve).

Further, distinctly slowed state-filling dynamics are revealed at reduced temperatures (Figure 4c). The peak of the MD emission (red) generally lags that of the ED emission (blue) by approximately 200 ps at the lowest temperatures, indicating a formation mechanism that is inhibited at low temperature.[45] The derived estimates of the energy barrier are in reasonable agreement with results from related systems with self-trapped excitons. For example, E_b is known to decrease with decreasing dimensionality. In 3D alkali halides, E_b is estimated to be ~20−30 meV.[45] In the 1D limit, the barrier vanishes[37,54] and the s exciton no longer represents a metastable state. In corrugated perovskites, an intermediate case between 2D and 1D, E_b is estimated to be less than 4 meV.[20] The values derived here at the lower temperatures lie between the 3D and corrugated materials, as expected.

Distinct Hysteresis of the MD around Structural Phase Transitions. Similar sample- and temperature-dependent behavior is observed in 2D HOIPs incorporating a variety of alkylammonium cations, such as butylammonium lead iodide (BA_2PbI_4) (Figure 5 and Figure S12). These other materials, however, exhibit structural phase transitions[47] at which abrupt changes in the PL spectra occur. These

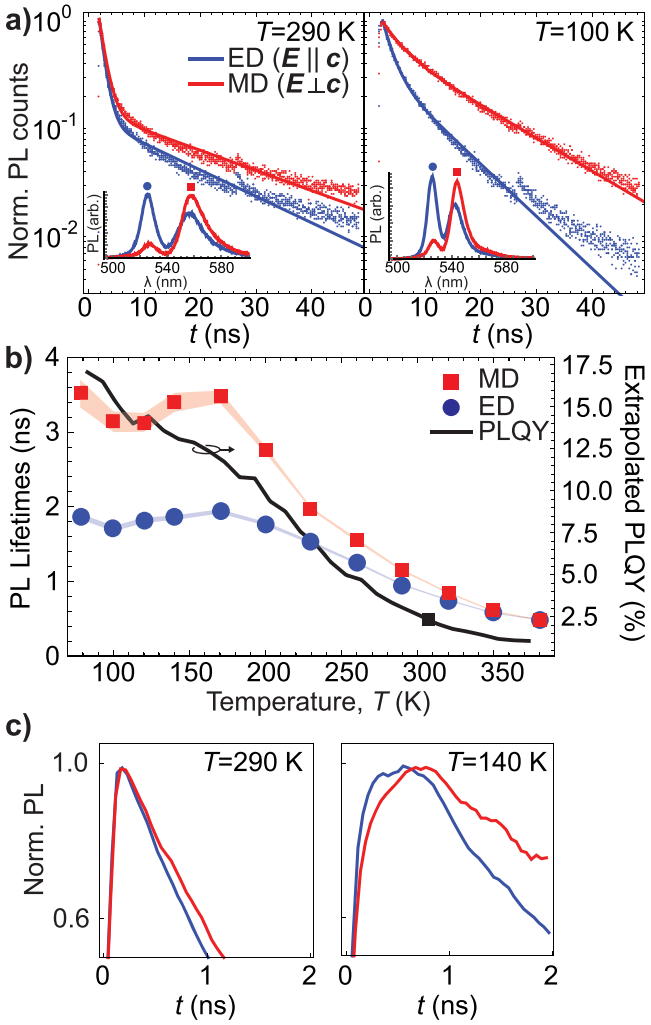

Figure 4. Isolating excited-state dynamics. (a) Photoluminescence decay traces of the spectrally isolated (blue) ED and (red) MD features at (left panel) 290 and 100 K, measured from a large as-grown single crystal using the edge-collection geometry, as illustrated in Figure 1a. Insets show the corresponding (blue) out-of-plane and (red) in-plane polarized photoluminescence spectra; solid markers specify the wavelengths at which decay traces were measured. The secondary small bump around 27 ns in measured decay traces arises from an internal reflection in the system and was ignored in the fitting. (b) Fit photoluminescence lifetimes, τ_1, of the (blue circles) ED and (red squares) MD. Confidence intervals (1σ) are represented by filled color regions. The solid black line represents the photoluminescence quantum yield (right axis) extrapolated from an integrating sphere measurement at 20 °C (black square) (Methods). (c) PL decay traces (linear scale) around the PL onset at (left) 290 K and (right) 140 K, showing significant differences in photoluminescence peak delays at lower temperatures.

discontinuities complicate analyses but also offer additional insights into the nature of the MD-emitting state.

For example, Figure 5a shows temperature-dependent PL spectra from oriented single crystals of BA_2PbI_4 upon heating from 173 K. Distinct ED and MD emission features can again be identified by comparing single crystals to randomly oriented fragments (Figure 5a,b). Like in PEA_2PbI_4, in any single phase, the ED peak is stable (Figure S12), whereas the MD exhibits large variations with temperature. Unlike PEA_2PbI_4, however, a structural phase transition occurs upon heating (Figure 5a,b) at

https://dx.doi.org/10.1021/acsnano.0c03783
ACS Nano 2020, 14, 8958−8968

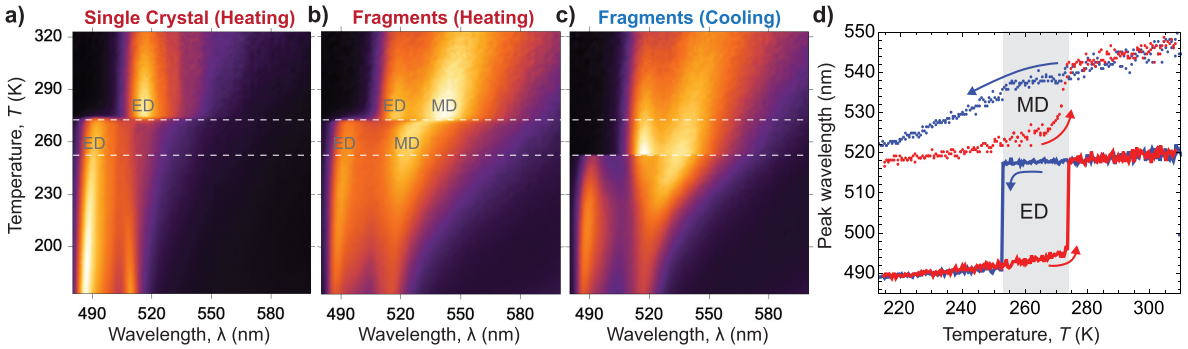

Figure 5. Temperature-dependent PL from BA_2PbI_4. (a) Single crystals upon heating. (b,c) Fragments upon (b) heating and (c) cooling. Horizontal white dashed lines highlight the phase transition temperatures inferred from cooling (bottom line) and heating (top line) data. (d) Peak wavelengths of ED (solid lines) and MD (dots) inferred from cooling (blue) and (red) heating data.

273 K and upon cooling (Figure 5c) at 253 K (Figure S13).[47] Interestingly, the MD exhibits significantly different behavior than the ED around the phase transitions. This contrasting behavior is highlighted in Figure 5d, where the ED (solid curves) and MD (dots) peak wavelengths are recorded during heating (red) and cooling (blue). The ED wavelength exhibits sharp discontinuities upon both heating and cooling. The MD wavelength, in contrast, varies continuously through the phase transition, particularly when cooling. Moreover, the ED only exhibits hysteretic behavior within a 20 K temperature band (gray region), whereas the MD remains hysteretic down to the lowest temperatures measured. We note that a residual ED peak at 518 nm exists below the phase transition temperature upon cooling (Figure 5c), suggesting partial phase conversion, which eventually vanishes upon further cooling. This, however, likely cannot explain the continuous variations observed in the MD emission.

We hypothesize that this unusual MD behavior reflects the self-trapping lattice distortion. Due to the local distortion, the self-trapped state is associated with a non-equilibrium lattice configuration and is thus weakly sensitive to abrupt changes in the host material's global structure. This may offer an intriguing avenue for future studies of non-equilibrium energy transfer or local dynamics that can be easily optically interrogated. It also highlights a photoresponsivity feature in BA_2PbI_4 that may be explored for hysteresis-based memory with optical accessibility just below room temperature.[55,56]

CONCLUSIONS

We show how MD light emission in 2D perovskites is well-explained by strong exciton−lattice interactions between a p-like exciton and a symmetric lattice distortion. The proposed electronic configuration of the stabilized MD-emitting state is consistent with the parity-broken, or "off-center" exciton, known in related systems.[26,37,40,42] Specifically, we exploit sample orientation to isolate and study the temperature dependence of ED- and MD-emitting excited states in 2D HOIPs. The PL ratio is successfully described by Boltzmann statistics in the presence of a ground-state configurational energy difference of $E_Q \approx 27$ meV, strongly suggesting that MD emission arises from a locally distorted lattice structure.

Experimentally observed MD thermal red shifts are described by an exciton−lattice coupling parameter (α_2) that increases with temperature due to lattice softening. Setting model parameters to match experimental spectra yields fit-free barrier energies that explain well the observed variations in ED and MD PL decay traces at low temperature. The attribution of MD emission to a locally distorted excited-state structure is bolstered by the observation of unusual MD hysteresis surrounding the structural phase transition in BA_2PbI_4. These results and analyses explain the origins of highly unusual MD emission in 2D HOIPs and highlight a feature of 2D HOIP excitons that may be useful for optically accessible hysteresis-based memory. Further detailed studies of population dynamics, such as by polarization-resolved transient absorption or optical Kerr effect,[57] would be particularly promising for understanding in greater detail the formation mechanism of the self-trapped state and its relationship to specific lattice modes. Overall, this work establishes a microscopic model for the dynamic formation of parity-broken states that lead to MD light−matter interactions in these materials. This may point toward methods of engineering, manipulating, or exploiting distinct ED and MD emission characteristics for photonic devices.

METHODS

Sample Preparation. Large crystals of PEA_2PbI_4 and BA_2PbI_4 were grown using the antisolvent vapor-assisted crystal growth technique described in ref 46. All solutions were prepared, stored, and deposited in a nitrogen-vacated glovebox. Solutions were deposited on 0.18 mm glass coverslips after a sequence of acetone/isopropyl alcohol cleaning and plasma treatment. Crystals were allowed to grow for at least 48 h. The two substrates were separated using a sterile needle and were subsequently lightly thermally annealed (at approximately 70 °C for 10−30 min) to remove residual solvent before removing for measurement. The resulting samples were very similar to those shown in ref 46. Exemplary crystals used for our PL measurements are shown in Figure S1. For single-crystal PL measurements (*e.g.*, temperature-dependent PL and time-resolved PL), the resulting crystals were measured without further processing. For measurements of randomly oriented fragments (*e.g.*, temperature-dependent PL), such crystals were scraped from the original substrate and collected upon a second substrate. For momentum-resolved PL (*e.g.*, Figures S2 and S3), as-grown crystals were mechanically exfoliated using Scotch tape and deposited on new 0.018 mm glass coverslips. Measured flakes were approximately 60 nm thick, as determined by atomic force microscopy.

Momentum-Resolved PL Spectra. Momentum-resolved PL spectra were collected from mechanically exfoliated flakes using the methods thoroughly described in ref 13. Briefly, an inverted microscope and a 1.3 NA oil-immersion objective were used to collect PL emitted from single exfoliated flakes of 2D HOIPs. Samples were excited with a focused 405 nm laser through the same objective. Excitation intensities were approximately 5 mW/cm^2. The momentum distribution of the PL was projected to the entrance slit of an

https://dx.doi.org/10.1021/acsnano.0c03783
ACS Nano 2020, 14, 8958−8968

imaging spectrometer using Fourier imaging techniques. The $k_{\|}$ distribution of PL was spectrally separated using a 300 g/mm grating, and the resulting 2D $\lambda-k_{\|}$ image was collected on a 1024 × 1024 CCD array. The s-polarized and p-polarized spectra were obtained by applying a linear polarizer to the collection side with horizontal and vertical alignments, respectively (*e.g.*, see Figure S2). High- and low-momentum spectra were extracted from the resulting 2D PL image.

Measuring Orientation Dependence of PL in Conventional Fluorimeter Geometry. Orientation-dependent PL (*e.g.*, Figure 1a) was collected from as-grown samples strategically positioned in the main chamber of a Horiba spectrometer (FluoroMax 4) in a 90° excitation-collection geometry. For "face" measurements, spectra were collected at approximately 30° from the substrate/sample normal (and thus excited at approximately 60° from the substrate normal). For "edge" measurements, spectra were collected from the edge of the substrate/sample at 90° from the substrate/sample normal (*i.e.*, excited at normal incidence). In-plane and out-of-plane polarized spectra were collected using a linear polarizer oriented either parallel to or perpendicular to the length of the substrate/sample. Samples were excited at 400 nm. We note that the relative intensities depend strongly on the position and angle of the sample, which accounts for the differences between momentum-resolved PL spectra and edge-collection spectra. Differences in the peak wavelength arise, in part, from increased temperatures in the sample chamber (described further below), with additional possible contributions from the overall higher quality and different dielectric environment inherent to the thick, as-grown single crystal.[58]

Measuring Temperature-Dependent PL. Temperature-dependent PL spectra of as-grown crystals and fragments were measured from samples placed in an evacuated temperature-controlled microscope stage (Linkam HFS600E-P) using one of the two experimental geometries illustrated in Figure 1b. Note that this approach, as opposed to the edge-collection geometry (Figure 1a), was used in this case primarily because the particular orthogonal window cryostat available to us was not conducive to continuous-temperature PL measurements. To ensure good thermal contact between the temperature-controlled drum and the sample, crystals were sealed between double-sided copper tape and the substrate, and the copper tape was adhered directly to the temperature-controlled drum. Samples were sealed in the cryostat using transparent glass windows and were evacuated to approximately 0.03 Torr. The sealed cryostat was positioned ("upside down") in the focal plane above a 10× NA = 0.3 objective (Nikon) of an inverted microscope (Nikon Eclipse Ti series). Samples were illuminated using a loosely focused (≈25−50 μm beam diameter) 405 nm laser with incident intensities of approximately 5−10 mW/cm^2, from which we predict excitation densities no greater than ∼10^{12} cm^{-3} and negligible sample heating. For oriented single-crystal measurements (*e.g.*, Figure 1b), single crystals approximately 100 μm in lateral extent were identified by eye and illuminated such that the focused excitation/PL spot was visually completely contained within the crystal. Collected PL was focused to the entrance aperture of an imaging spectrometer and was spatially filtered to contain only the PL emitted from the excitation spot (*e.g.*, eliminating light emitted toward and scattered from crystal edges). For randomly oriented fragments, identical illumination and collection conditions were used on samples prepared according to the description in Sample Preparation. Spectra were continuously collected in this manner while the sample temperature varied at a rate of approximately 5 °C/min. Measurements performed at 0.5, 1, 2, and 3 °C/min revealed similar behavior and phase transition temperatures, ensuring that the observed hysteresis is indeed a material phenomenon rather than an experimental artifact (*e.g.*, see Figure S13). Exposure times varied from 1 s at lower temperatures (where photoluminescence quantum yields, PLQYs, are larger) to 10 s at higher temperatures (where PLQYs are lower). The resulting temperature resolution is thus approximately 0.1−1.0 °C per spectrum. Spectra were collected upon both cooling and heating over the entire temperature range twice to ensure consistency. Spectra in all cases were qualitatively similar.

Decomposing Temperature-Dependent Spectra. Temperature-dependent PL (*e.g.*, Figure 2a and Figure S4a) were decomposed at each temperature independently into a sum of phenomenological asymmetric line shapes of the form $I_{PL}(\lambda) = A\,\mathrm{sech}[(\lambda - \lambda_0)/\sigma]$. This line shape is not intended to directly address broadening mechanisms, such as those in ref 59, but rather to provide reliable estimates of the center wavelengths and total PL originating from each of the two emission features of interest here. To account for the asymmetry, the width σ was allowed to differ between the left and right side of the center, λ_0, taking a value σ_L on the left ($\lambda < \lambda_0$) and σ_R on the right ($\lambda > \lambda_0$). With this, we first fit single-crystal data to a single such contribution (ED) to obtain at each temperature the four parameters associated with the ED: $A_{ED}(T)$, $\lambda_{0,ED}(T)$, $\sigma_{L,ED}(T)$, and $s_{ED}(T)$. We then fit the fragments data to a sum of two contributions (ED and MD), inputting the predetermined values $\lambda_{0,ED}(T)$, $\sigma_{L,ED}(T)$, and $s_{ED}(T)$. To minimize the number of free parameters, a single proportionality constant, s_{MD}, was chosen to best represent the MD emission over all temperatures (s_{MD} = 1.55). From two-component fits, we obtain $A_{ED}(T)$, $A_{MD}(T)$, $\lambda_{0,MD}(T)$, and $\sigma_{L,MD}(T)$. A_{ED} must be allowed to vary during two-component fits to account for variations in experimental setup and sample geometry between single crystals and fragments. Exemplary fits from PEA_2PbI_4 are shown in Figure S4 and show excellent agreement with the data.

Time-Resolved PL. Time-correlated single-photon counting measurements were performed in the UCSB Optical Characterization Facility. An edge-collection geometry, as illustrated in Figure 1a, was used. As-grown crystals (see Sample Preparation) were mounted within an evacuated cryostat (Janis Research) maintained at approximately 0.5 × 10^{-5} mBar and passively cooled with liquid nitrogen to approximately 78 K. Samples were pumped at normal incidence at 405 nm with approximately 0.025 μJ/cm^2 per pulse with a 20 MHz repetition rate. PL decay traces were collected from the edge of the substrate (from which the optically pumped crystal was no greater than 1 mm), analogous to edge measurements performed in the fluorimeter, described above. PL decay traces were recorded at the spectral position of the ED and MD maxima (*e.g.*, 525 nm for the ED and between approximately 540 and 560 nm for the MD, depending on temperature). A linear polarizer was applied on the collection side with in-plane or out-of-plane polarizer alignment to further isolate the MD and ED, respectively, for each measurement. PL decay traces at each temperature were fit to a two-component exponential decay. The ED and MD were identified as the short-lived components at each temperature.

Measuring and Extrapolating PLQY. PLQY of PEA_2PbI_4 single crystals was measured using a Horiba spectrometer (FluoroMax 4) and integrating sphere (Horiba Quanta-ϕ) with 405 nm wavelength excitation. Crystals (approximately 2 mm in lateral extent, several hundred micrometers thick) grown using the methods described above were transferred to fused silica substrates and positioned on the sample plug of the integrating sphere. The number of absorbed photons was determined with a 1 s exposure by collecting over the excitation line of the attenuated beam (nominal OD = 3, measured attenuation factor 610.8) with the sample in place and comparing to a non-absorbing reference (blank sample plug), measured with identical excitation and collection parameters. The total PL counts was determined by collecting over the PL band and subtracting instrument noise due to Rayleigh scattering, measured with identical excitation and collection parameters (except the OD = 3 filter). Measurement was performed at room temperature (assumed to be 300 K). PLQY was extrapolated to low and high temperatures using un-normalized temperature-dependent PL data from as-grown single crystals under the assumption that the radiative (nonradiative) rate is invariant (varies) with temperature.

ASSOCIATED CONTENT

Supporting Information

The Supporting Information is available free of charge at https://pubs.acs.org/doi/10.1021/acsnano.0c03783.

https://dx.doi.org/10.1021/acsnano.0c03783
ACS Nano 2020, 14, 8958−8968

Supporting discussion, theoretical details, and figures (PDF)

AUTHOR INFORMATION

Corresponding Author

Jon A. Schuller − *Department of Electrical and Computer Engineering, University of California Santa Barbara, Santa Barbara, California 93106, United States;* orcid.org/0000-0001-6949-3569; Email: jonschuller@ece.ucsb.edu

Authors

Ryan A. DeCrescent − *Department of Physics, University of California Santa Barbara, Santa Barbara, California 93106, United States;* orcid.org/0000-0003-3219-7736

Xinhong Du − *Department of Electrical and Computer Engineering, University of California Santa Barbara, Santa Barbara, California 93106, United States*

Rhys M. Kennard − *Department of Materials, University of California Santa Barbara, Santa Barbara, California 93106, United States*

Naveen R. Venkatesan − *Department of Materials, University of California Santa Barbara, Santa Barbara, California 93106, United States;* orcid.org/0000-0003-2086-5274

Clayton J. Dahlman − *Department of Materials, University of California Santa Barbara, Santa Barbara, California 93106, United States;* orcid.org/0000-0002-4555-4846

Michael L. Chabinyc − *Department of Materials, University of California Santa Barbara, Santa Barbara, California 93106, United States;* orcid.org/0000-0003-4641-3508

Complete contact information is available at: https://pubs.acs.org/10.1021/acsnano.0c03783

Notes

The authors declare no competing financial interest.

ACKNOWLEDGMENTS

This work, including all optical measurements, analyses, and theoretical modeling, was primarily supported as part of Quantum Materials for Energy Efficient Neuromorphic Computing, an Energy Frontier Research Center funded by the U.S. Department of Energy (DOE), Office of Science, Basic Energy Sciences (BES), under Award Number DE-SC0019273. Materials synthesis and structural characterization were supported by the U.S. Department of Energy, Office of Science, Basic Energy Sciences, under Award Number DE-SC-0012541. The research reported here also made use the shared facilities of the UCSB MRSEC (National Science Foundation DMR 1720256), a member of the Materials Research Facilities Network (www.mrfn.org). R.M.K. gratefully acknowledges the National Defense Science and Engineering Graduate fellowship for financial support.

REFERENCES

(1) Berry, J.; Buonassisi, T.; Egger, D. A.; Hodes, G.; Kronik, L.; Loo, Y.-L.; Lubomirsky, I.; Marder, S. R.; Mastai, Y.; Miller, J. S.; Mitzi, D. B.; Paz, Y.; Rappe, A. M.; Riess, I.; Rybtchinski, B.; Stafsudd, O.; Stevanovic, V.; Toney, M. F.; Zitoun, D.; Kahn, A.; et al. Hybrid Organic-Inorganic Perovskites (HOIPs): Opportunities and Challenges. *Adv. Mater.* **2015**, *27*, 5102−5112.

(2) Zhang, W.; Eperon, G. E.; Snaith, H. J. Metal Halide Perovskites for Energy Applications. *Nat. Energy* **2016**, *1*, 16048.

(3) Ishihara, T.; Takahashi, J.; Goto, T. Optical Properties Due to Electronic Transitions in Two-Dimensional Semiconductors $(C_nH_{2n+1}NH_3)_2PbI_4$. *Phys. Rev. B: Condens. Matter Mater. Phys.* **1990**, *42*, 11099−11107.

(4) Mitzi, D. B. Synthesis, Crystal Structure, and Optical and Thermal Properties of $(C_4H_9NH_3)_2MI_4$ (M = Ge, Sn, Pb). *Chem. Mater.* **1996**, *8*, 791−800.

(5) Tanaka, K.; Takahashi, T.; Kondo, T.; Umeda, K.; Ema, K.; Umebayashi, T.; Asai, K.; Uchida, K.; Miura, N. Electronic and Excitonic Structures of Inorganic-Organic Perovskite-Type Quantum-Well Crystal $(C_4H_9NH_3)_2PbBr_4$. *Jpn. J. Appl. Phys.* **2005**, *44*, 5923.

(6) Smith, I. C.; Hoke, E. T.; Solis-Ibarra, D.; McGehee, M. D.; Karunadasa, H. I. A Layered Hybrid Perovskite Solar-Cell Absorber with Enhanced Moisture Stability. *Angew. Chem.* **2014**, *126*, 11414−11417.

(7) Tsai, H.; Nie, W.; Blancon, J.-C.; Stoumpos, C. C.; Asadpour, R.; Harutyunyan, B.; Neukirch, A. J.; Verduzco, R.; Crochet, J. J.; Tretiak, S.; Pedesseau, L.; Even, J.; Alam, M. A.; Gupta, G.; Lou, J.; Ajayan, P. M.; Bedzyk, M. J.; Kanatzidis, M. G.; Mohite, A. D. High-Efficiency Two-Dimensional Ruddlesden-Popper Perovskite Solar Cells. *Nature* **2016**, *536*, 312−316.

(8) Katan, C.; Mercier, N.; Even, J. Quantum and Dielectric Confinement Effects in Lower-Dimensional Hybrid Perovskite Semiconductors. *Chem. Rev.* **2019**, *119*, 3140−3192.

(9) Tanaka, K.; Takahashi, T.; Kondo, T.; Umebayashi, T.; Asai, K.; Ema, K. Image Charge Effect on Two-Dimensional Excitons in an Inorganic-Organic Quantum-Well Crystal. *Phys. Rev. B: Condens. Matter Mater. Phys.* **2005**, *71*, 045312.

(10) Lanty, G.; Bréhier, A.; Parashkov, R.; Lauret, J. S.; Deleporte, E. Strong Exciton-Photon Coupling at Room Temperature in Microcavities Containing Two-Dimensional Layered Perovskite Compounds. *New J. Phys.* **2008**, *10*, 065007.

(11) Stranks, S. D.; Plochocka, P. The Influence of the Rashba Effect. *Nat. Mater.* **2018**, *17*, 381−382.

(12) Fieramosca, A.; Polimeno, L.; Ardizzone, V.; De Marco, L.; Pugliese, M.; Maiorano, V.; De Giorgi, M.; Dominici, L.; Gigli, G.; Gerace, D.; Ballarini, D.; Sanvitto, D. Two-Dimensional Hybrid Perovskites Sustaining Strong Polariton Interactions at Room Temperature. *Sci. Adv.* **2019**, *5*, No. eaav9967.

(13) DeCrescent, R. A.; Venkatesan, N. R.; Dahlman, C. J.; Kennard, R. M.; Zhang, X.; Li, W.; Du, X.; Chabinyc, M. L.; Zia, R.; Schuller, J. A. Bright Magnetic Dipole Radiation from Two-Dimensional Lead-Halide Perovskites. *Sci. Adv.* **2020**, *6*, No. eaay4900.

(14) Kovalenko, M. V.; Protesescu, L.; Bodnarchuk, M. I. Properties and Potential Optoelectronic Applications of Lead Halide Perovskite Nanocrystals. *Science* **2017**, *358*, 745−750.

(15) Srimath Kandada, A. R.; Silva, C. Exciton Polarons in Two-Dimensional Hybrid Metal-Halide Perovskites. *J. Phys. Chem. Lett.* **2020**, *11*, 3173−3184.

(16) Smith, M. D.; Karunadasa, H. I. White-Light Emission from Layered Halide Perovskites. *Acc. Chem. Res.* **2018**, *51*, 619−627.

(17) Moral, R. F.; Bonato, L. G.; Germino, J. C.; Coelho Oliveira, W. X.; Kamat, R.; Xu, J.; Tassone, C. J.; Stranks, S. D.; Toney, M. F.; Nogueira, A. F. Synthesis of Polycrystalline Ruddlesden-Popper Organic Lead Halides and Their Growth Dynamics. *Chem. Mater.* **2019**, *31*, 9472−9479.

(18) Maczka, M.; Ptak, M.; Gagor, A.; Stefanska, D.; Sieradzki, A. Layered Lead Iodide of $[(Methylhydrazinium]_2PbI_4$ with a Reduced Band Gap: Thermochromic Luminescence and Switchable Dielectric Properties Triggered by Structural Phase Transitions. *Chem. Mater.* **2019**, *31*, 8563−8575.

(19) Gautier, R.; Paris, M.; Massuyeau, F. Exciton Self-Trapping in Hybrid Lead Halides: Role of Halogen. *J. Am. Chem. Soc.* **2019**, *141*, 12619−12623.

(20) Hu, T.; Smith, M. D.; Dohner, E. R.; Sher, M.-J.; Wu, X.; Trinh, M. T.; Fisher, A.; Corbett, J.; Zhu, X.-Y.; Karunadasa, H. I.; Lindenberg, A. M. Mechanism for Broadband White-Light Emission from Two-Dimensional (110) Hybrid Perovskites. *J. Phys. Chem. Lett.* **2016**, *7*, 2258−2263.

(21) Gauthron, K.; Lauret, J-S.; Doyennette, L.; Lanty, G.; Al Choueiry, A.; Zhang, S. J.; Brehier, A.; Largeau, L.; Mauguin, O.;

Bloch, J.; Deleporte, E. Optical Spectroscopy of Two-Dimensional Layered $(C_6H_5C_2H_4\text{-}NH_3)_2\text{-}PbI_4$ Perovskite. *Opt. Express* **2010**, *18*, 5912−5919.
(22) Stoumpos, C. C.; Cao, D. H.; Clark, D. J.; Young, J.; Rondinelli, J. M.; Jang, J. I.; Hupp, J. T.; Kanatzidis, M. G. Ruddlesden-Popper Hybrid Lead Iodide Perovskite 2D Homologous Semiconductors. *Chem. Mater.* **2016**, *28*, 2852−2867.
(23) Guo, P.; Huang, W.; Stoumpos, C. C.; Mao, L.; Gong, J.; Zeng, L.; Diroll, B. T.; Xia, Y.; Ma, X.; Gosztola, D. J.; Xu, T.; Ketterson, J. B.; Bedzyk, M. J.; Facchetti, A.; Marks, T. J.; Kanatzidis, M. G.; Schaller, R. D. Hyperbolic Dispersion Arising from Anisotropic Excitons in Two-Dimensional Perovskites. *Phys. Rev. Lett.* **2018**, *121*, 127401.
(24) Wang, S.; Ma, J.; Li, W.; Wang, J.; Wang, H.; Shen, H.; Li, J.; Wang, J.; Luo, H.; Li, D. Temperature-Dependent Band Gap in Two-Dimensional Perovskites: Thermal Expansion Interaction and Electron-Phonon Interaction. *J. Phys. Chem. Lett.* **2019**, *10*, 2546−2553.
(25) Even, J.; Pedesseau, L.; Dupertuis, M.-A.; Jancu, J.-M.; Katan, C. Electronic Model for Self-Assembled Hybrid Organic/Perovskite Semiconductors: Reverse Band Edge Electronic States Ordering and Spin-Orbit Coupling. *Phys. Rev. B: Condens. Matter Mater. Phys.* **2012**, *86*, 205301.
(26) Noba, K.-i.; Kayanuma, Y. Model for Self-Trapping of Excitons with Internal Degrees of Freedom. *J. Phys. Soc. Jpn.* **1998**, *67*, 3388−3391.
(27) Bunker, P. R.; Jensen, P. *Molecular Symmetry and Spectroscopy*, 1st ed.; Academic Press: New York, 1979; Chapter 11, pp 268−328.
(28) Pelant, I.; Valenta, J. *Luminescence Spectroscopy of Semiconductors*; OUP Oxford: Oxford, England, 2012; Chapter 7, pp 161−202.
(29) Wang, G.; Robert, C.; Glazov, M.; Cadiz, F.; Courtade, E.; Amand, T.; Lagarde, D.; Taniguchi, T.; Watanabe, K.; Urbaszek, B.; Marie, X. In-Plane Propagation of Light in Transition Metal Dichalcogenide Monolayers: Optical Selection Rules. *Phys. Rev. Lett.* **2017**, *119*, 047401.
(30) Yaffe, O.; Guo, Y.; Tan, L. Z.; Egger, D. A.; Hull, T.; Stoumpos, C. C.; Zheng, F.; Heinz, T. F.; Kronik, L.; Kanatzidis, M. G.; Owen, J. S.; Rappe, A. M.; Pimenta, M. A.; Brus, L. E. Local Polar Fluctuations in Lead Halide Perovskite Crystals. *Phys. Rev. Lett.* **2017**, *118*, 136001.
(31) McKechnie, S.; Frost, J. M.; Pashov, D.; Azarhoosh, P.; Walsh, A.; van Schilfgaarde, M. Dynamic Symmetry Breaking and Spin Splitting in Metal Halide Perovskites. *Phys. Rev. B: Condens. Matter Mater. Phys.* **2018**, *98*, 085108.
(32) Niesner, D.; Hauck, M.; Shrestha, S.; Levchuk, I.; Matt, G. J.; Osvet, A.; Batentschuk, M.; Brabec, C.; Weber, H. B.; Fauster, T. Structural Fluctuations Cause Spin-Split States in Tetragonal $(CH_3NH_3)PbI_3$ as Evidenced by the Circular Photogalvanic Effect. *Proc. Natl. Acad. Sci. U. S. A.* **2018**, *115*, 9509−9514.
(33) Zheng, C.; Yu, S.; Rubel, O. Structural Dynamics in Hybrid Halide Perovskites: Bulk Rashba Splitting, Spin Texture, and Carrier Localization. *Phys. Rev. Mater.* **2018**, *2*, 114604.
(34) Bechtel, J. S.; Van der Ven, A. Octahedral Tilting Instabilities in Inorganic Halide Perovskites. *Phys. Rev. Mater.* **2018**, *2*, 025401.
(35) Schmitt, T.; Bourelle, S.; Tye, N.; Soavi, G.; Bond, A. D.; Feldmann, S.; Traore, B.; Katan, C.; Even, J.; Dutton, S. E.; Deschler, F. Control of Crystal Symmetry Breaking with Halogen-Substituted Benzylammonium in Layered Hybrid Metal-Halide Perovskites. *J. Am. Chem. Soc.* **2020**, *142*, 5060−5067.
(36) Blancon, J.-C.; Stier, A. V.; Tsai, H.; Nie, W.; Stoumpos, C. C.; Traore, B.; Pedesseau, L.; Kepenekian, M.; Katsutani, F.; Noe, G. T.; Kono, J.; Tretiak, S.; Crooker, S. A.; Katan, C.; Kanatzidis, M. G.; Crochet, J. J.; Even, J.; Mohite, A. D. Scaling Law for Excitons in 2D Perovskite Quantum Wells. *Nat. Commun.* **2018**, *9*, 2254.
(37) Toyozawa, Y. Excitonic Instabilities of Deformable Lattice - From Self-Trapping to Phase Transition. *Acta Phys. Pol., A* **1995**, *87*, 47−56.
(38) Cortecchia, D.; Yin, J.; Bruno, A.; Lo, S.-Z. A.; Gurzadyan, G. G.; Mhaisalkar, S.; Brédas, J.-L.; Soci, C. Polaron Self-Localization in White-Light Emitting Hybrid Perovskites. *J. Mater. Chem. C* **2017**, *5*, 2771−2780.
(39) Messerschmidt, S.; Krampf, A.; Freytag, F.; Imlau, M.; Vittadello, L.; Bazzan, M.; Corradi, G. The Role of Self-Trapped Excitons in Polaronic Recombination Processes in Lithium Niobate. *J. Phys.: Condens. Matter* **2019**, *31*, 065701.
(40) Wang, X.; Meng, W.; Liao, W.; Wang, J.; Xiong, R.-G.; Yan, Y. Atomistic Mechanism of Broadband Emission in Metal Halide Perovskites. *J. Phys. Chem. Lett.* **2019**, *10*, 501−506.
(41) Nishimura, H.; Yamaoka, T.; Mizuno, K.-i.; Iemura, M.; Matsui, A. Luminescence of Free and Self-Trapped Excitons in α- and β-Perylene Crystals. *J. Phys. Soc. Jpn.* **1984**, *53*, 3999−4008.
(42) Williams, R. T.; Song, K. S.; Faust, W. L.; Leung, C. H. Off-Center Self-Trapped Excitons and Creation of Lattice Defects in Alkali Halide Crystals. *Phys. Rev. B: Condens. Matter Mater. Phys.* **1986**, *33*, 7232−7240.
(43) Tanimura, K.; Itoh, N. Selective Non-Radiative Transitions at Excited States of the Self-Trapped Exciton in Alkali Halides. *J. Phys. Chem. Solids* **1984**, *45*, 323−340.
(44) Smith, M. D.; Jaffe, A.; Dohner, E. R.; Lindenberg, A. M.; Karunadasa, H. I. Structural Origins of Broadband Emission from Layered Pb-Br Hybrid Perovskites. *Chem. Sci.* **2017**, *8*, 4497−4504.
(45) Unuma, Y.; Masumoto, Y.; Shionoya, S.; Nishimura, H. Dynamical Aspects of Self-Trapping of 1s Excitons in RbI and KI. *J. Phys. Soc. Jpn.* **1983**, *52*, 4277−4282.
(46) Lédée, F.; Trippé-Allard, G.; Diab, H.; Audebert, P.; Garrot, D.; Lauret, J.-S.; Deleporte, E. Fast Growth of Monocrystalline Thin Films of 2D Layered Hybrid Perovskite. *CrystEngComm* **2017**, *19*, 2598−2602.
(47) Billing, D. G.; Lemmerer, A. Synthesis, Characterization and Phase Transitions in the Inorganic-Organic Layered Perovskite-Type Hybrids $[(C_nH_{2n+1}NH_3)_2PbI_4]$, n = 4, 5 and 6. *Acta Crystallogr., Sect. B: Struct. Sci.* **2007**, *63*, 735−747.
(48) Rudin, S.; Reinecke, T. L.; Segall, B. Temperature-Dependent Exciton Linewidths in Semiconductors. *Phys. Rev. B: Condens. Matter Mater. Phys.* **1990**, *42*, 11218−11231.
(49) Wright, A. D.; Verdi, C.; Milot, R. L.; Eperon, G. E.; Pérez-Osorio, M. A.; Snaith, H. J.; Giustino, F.; Johnston, M. B.; Herz, L. M. Electron-Phonon Coupling in Hybrid Lead Halide Perovskites. *Nat. Commun.* **2016**, *7*, 11755.
(50) Kitazawa, N.; Aono, M.; Watanabe, Y. Temperature-Dependent Time-Resolved Photoluminescence of $(C_6H_5C_2H_4NH_3)_2PbX_4$ (X = Br and I). *Mater. Chem. Phys.* **2012**, *134*, 875−880.
(51) Marshall, B. J.; Pederson, D. O.; Dorris, G. G. Elastic Constants of LiCl and RbCl from 300 to 4.2 K. *J. Phys. Chem. Solids* **1967**, *28*, 1061.
(52) Mohamed, R. M.; Mishra, M. K.; AL-Harbi, L. M.; Al-Ghamdi, M. S.; Asiri, A. M.; Reddy, C. M.; Ramamurty, U. Temperature Dependence of Mechanical Properties in Molecular Crystals. *Cryst. Growth Des.* **2015**, *15*, 2474−2479.
(53) Liu, S.; Sun, S.; Gan, C. K.; del Águila, A. G.; Fang, Y.; Xing, J.; Do, T. T. H.; White, T. J.; Li, H.; Huang, W.; Xiong, Q. Manipulating Efficient Light Emission in Two-Dimensional Perovskite Crystals by Pressure-Induced Anisotropic Deformation. *Sci. Adv.* **2019**, *5*, No. eaav9445.
(54) Tomimoto, S.; Nansei, H.; Saito, S.; Suemoto, T.; Takeda, J.; Kurita, S. Femtosecond Dynamics of the Exciton Self-Trapping Process in a Quasi-One-Dimensional Halogen-Bridged Platinum Complex. *Phys. Rev. Lett.* **1998**, *81*, 417−420.
(55) Ríos, C.; Stegmaier, M.; Hosseini, P.; Wang, D.; Scherer, T.; Wright, C. D.; Bhaskaran, H.; Pernice, W. H. P. Integrated All-Photonic Non-Volatile Multi-Level Memory. *Nat. Photonics* **2015**, *9*, 725−732.
(56) Tian, H.; Zhao, L.; Wang, X.; Yeh, Y.-W.; Yao, N.; Rand, B. P.; Ren, T.-L. Extremely Low Operating Current Resistive Memory Based on Exfoliated 2D Perovskite Single Crystals for Neuromorphic Computing. *ACS Nano* **2017**, *11*, 12247−12256.

https://dx.doi.org/10.1021/acsnano.0c03783
ACS Nano 2020, 14, 8958−8968

(57) Miyata, K.; Meggiolaro, D.; Trinh, M. T.; Joshi, P. P.; Mosconi, E.; Jones, S. C.; De Angelis, F.; Zhu, X.-Y. Large Polarons in Lead Halide Perovskites. *Sci. Adv.* **2017**, *3*, No. e1701217.
(58) Zhang, Q.; Chu, L.; Zhou, F.; Ji, W.; Eda, G. Excitonic Properties of Chemically Synthesized 2D Organic-Inorganic Hybrid Perovskite Nanosheets. *Adv. Mater.* **2018**, *30*, 1704055.
(59) Neutzner, S.; Thouin, F.; Cortecchia, D.; Petrozza, A.; Silva, C.; Srimath Kandada, A. R. Exciton-Polaron Spectral Structures in Two-Dimensional Hybrid Lead-Halide Perovskites. *Phys. Rev. Mater.* **2018**, *2*, 064605.

https://dx.doi.org/10.1021/acsnano.0c03783
ACS Nano 2020, 14, 8958−8968